Mon. Not. R. Astron. Soc. **283,** 892–904 (1996)

Green's matrix for Compton reflection of polarized radiation from cold matter

Juri Poutanen,[1]★ K. N. Nagendra[2]★ and Roland Svensson[1]★

[1] *Stockholm Observatory, S-133 36 Saltsjöbaden, Sweden*
[2] *Indian Institute of Astrophysics, Bangalore 560034, India*

Accepted 1996 July 15. Received 1996 July 15; in original form 1995 September 15

ABSTRACT

The Compton-reflected spectrum from cold matter for incident X-rays and γ-rays with arbitrary angular, spectral and polarization properties can be determined by a simple folding of Green's matrix with the incident spectrum. We calculate Green's matrix by numerically solving the polarized radiative transfer equation for an optically thick planar slab of neutral matter using a method based on discrete space theory. We account for both angular and polarization properties of the fully relativistic Compton scattering cross-section as well as photoelectric absorption and the generation of a fluorescent Fe line. We describe through simple models the basic characteristics of polarized spectra produced by Rayleigh and Compton scattering. The emphasis is on exact computations of Compton-reflected spectra. For the first time, the Fe line equivalent width can be calculated self-consistently for an arbitrary angular distribution of the incident spectrum using Green's matrix formalism.

Key words: polarization – radiative transfer – scattering – galaxies: Seyfert – gamma-rays: theory – X-rays: general.

1 INTRODUCTION

Observations ranging from soft X-rays to soft gamma-rays seem to indicate the existence of Compton reflection of X-rays by cold matter in different types of astronomical objects. These include Seyfert galaxies (e.g., Pounds et al. 1990, Nandra & Pounds 1994, Zdziarski et al. 1994, Zdziarski, Johnson & Magdziarz 1996), and X-ray binaries such as Cyg X-1 (Done et al. 1992; Haardt et al. 1993).

In the two-phase disc–corona models for Seyfert galaxies (e.g., Haardt & Maraschi 1993, Stern et al. 1995), hot coronal electrons produce the X-ray spectra by successive Compton scatterings of the low-energy photons from the accretion disc. The mildly relativistic temperatures of the coronal electrons together with the anisotropy of the low-energy disc photons (as they enter the corona from one side only) cause the Compton-scattered coronal X-ray spectrum (in particular at photon energies where the first scattering order dominates) to be angularly dependent. This requires that the theoretical Compton-reflected spectrum can be accurately calculated for angularly dependent incident coronal spectra at all photon energies of relevance, i.e. up to several hundred keV or more. Reflected spectra are necessarily polarized, and future prospects of utilizing polarized X-ray data as diagnostics can only be realized if polarized Compton-reflected spectra can be calculated. Several approaches have been used in the literature to compute the Compton-reflected spectrum for a given incident spectrum. They can broadly be divided into two groups: (i) full radiative transfer calculations and (ii) Green's function methods.

The full radiative transfer calculations have been performed using Monte Carlo methods (e.g., George & Fabian 1991, Matt, Perola & Piro 1991, Matt 1993) for a given incident spectrum and chosen geometry, normally a semi-infinite slab with semi-isotropic illumination either in flux (from, e.g., an optically thin coronal slab) or in intensity (from, e.g., an optically thick corona). The disadvantage of such transfer calculations is that a new simulation must be performed for each change in the properties of the incident spectrum. The method is therefore not suitable for fitting observed spectra.

In order to perform efficient spectral fitting, one needs a fast and simple method to compute the reflected spectrum given an incident spectrum. This can be done by convolving

★E-mail: juri@astro.su.se (JP); knn@iiap.ernet.in (KNN); svensson@astro.su.se (RS).

the incident spectrum with Green's function, $G(\nu, \mu; \nu', \mu')$, which describes the reflected spectrum at photon frequency, ν and cosine angle μ, for incident monochromatic photons at μ' and ν'. Two methods have been used to determine Green's function.

First, the radiative transfer is solved by separately considering transport in physical space and frequency space giving the escape probability and the spectral distribution after n scatterings (Illarionov et al. 1979; Lightman, Lamb & Rybicki 1981; Burigana 1995). Green's function is constructed by summing the product of the escape probability and the spectral distribution over all scattering orders. A number of approximations such as isotropic scattering in the Thomson limit, the decoupling of the transport in physical space and frequency space, and solving the radiative transfer in the two-stream approximation limits the validity of the results to photon energies < 50 keV.

Secondly, several authors (White, Lightman & Zdziarski 1988; Hua & Lingenfelter 1992; Magdziarz & Zdziarski 1995) have determined Green's function by fitting analytical functions to Monte Carlo results. These works do not determine the full $G(\nu, \mu; \nu', \mu')$, but make assumptions about the angular dependencies, at least for the incident radiation. In the most detailed work, Magdziarz & Zdziarski (1995) computed and fitted the angularly dependent $G(\nu, \mu; \nu')$ for isotropic incident flux showing the importance of considering angular dependencies. The reflected spectra are, for example, much harder at larger viewing angles (smaller μ).

The Compton scattering cross-section depends on the polarization state. As the dominant contribution to Green's function comes from photons scattered only a few times, the degree of polarization can be high directly affecting the reflected intensity. Polarized Compton reflection was only considered by Matt (1993), whose result was limited to a specific incident power-law spectrum, and Fernández et al. (1993), whose results are limited to incident monoenergetic photons.

In spite of all of the work summarized above, there still exists no method to compute the full Green's function, $G(\nu, \mu; \nu', \mu')$, that is also valid for photon energies larger than 100 keV and that considers the full angular dependence of both incident and reflected radiation. Furthermore, most works have only considered one single Green's function describing incident intensity being converted into reflected intensity. In order to treat the effects of linear polarization on the reflected spectrum one needs to know three additional Green's functions. These four Green's functions are the components of Green's matrix that converts an incident Stokes vector into a reflected Stokes vector.

In this paper, we compute Green's matrix describing Compton reflection from an optically thick planar slab of incident radiation with arbitrary spectral, angular and polarization properties by solving the radiative transfer equation using the discrete space theory of radiative transfer. We limit our calculations to incident photon energies of less than 4 MeV. This is not much of a limitation, as the observed spectra of Seyfert galaxies and X-ray binaries have cut-offs at a few hundred keV.

In Section 2 we discuss the radiative transfer equation. The redistribution matrices for Rayleigh scattering, Compton scattering and Fe line fluorescence are given in Section 3. In Section 4, we present the results of our radiative transfer calculations, considering the Compton reflection below and above 5 keV separately. We discuss several cases of incident radiation with different angular, spectral and polarization properties. Details of the radiative transfer algorithm are given in Appendix A.

2 RADIATIVE TRANSFER EQUATION

We consider Compton reflection from a semi-infinite homogeneous slab of cold neutral matter with cosmic abundances. We approximate the semi-infinite homogeneous slab with a finite slab of total Thomson optical depth large enough ($T > 100$) such that a negligible amount of radiation is transmitted. We use the following notations: $\tilde{\boldsymbol{I}} = (I, Q)^T$ is the Stokes vector (see Chandrasekhar 1960); the degree of polarization, $p \equiv Q/I \cdot 100$ per cent $= (I_l - I_r)/(I_l + I_r) \cdot 100$ per cent. We use I_l and I_r to denote the components of the intensity with the electric vector in the meridian plane and perpendicular to it, respectively. The meridian plane is defined by the direction of photon propagation and the normal to the slab. The polarization is positive when the electric vector is predominantly parallel to the meridian plane. We do not consider the Stokes V parameter, because there is no source of circular polarization and V is independent of the other Stokes parameters, I, Q and U. The third Stokes parameter, U, is equal to zero because of the azimuthal symmetry of the chosen geometry. The general form of the polarized radiative transfer equation in an axisymmetric plane-parallel medium is written as

$$\mu \frac{\mathrm{d}\tilde{\boldsymbol{I}}(\tau, x, \mu)}{\mathrm{d}\tau} = -\tilde{\boldsymbol{I}}(\tau, x, \mu) + \lambda(x) \int_0^\infty \left(\frac{x}{x'}\right) \mathrm{d}x' \int_{-1}^{1} \mathrm{d}\mu' \times \hat{\mathbf{R}}(x, \mu; x', \mu') \tilde{\boldsymbol{I}}(\tau, x', \mu'), \quad (1)$$

where μ is the cosine of the angle between the direction of photon propagation and the slab normal, $\mathrm{d}\tau = n_{\mathrm{H}}[\sigma_{\mathrm{ph}}(x) + \sigma_{\mathrm{sc}}(x)]\,\mathrm{d}z$ is the incremental vertical optical depth, $\sigma_{\mathrm{ph}}(x)$ is the photoelectric absorption cross-section (Morrison & McCammon 1983), $\sigma_{\mathrm{sc}}(x)$ is the scattering cross-section being the sum of a coherent, $\sigma_{\mathrm{coh}}(x)$, and an incoherent, $\sigma_{\mathrm{incoh}}(x)$, component (see Hubbel et al. 1975). Only hydrogen and helium contribute significantly to $\sigma_{\mathrm{sc}}(x)$. All cross-sections are defined per hydrogen atom. Furthermore, $x \equiv h\nu/m_e c^2$ is the dimensionless photon energy in units of the electron rest mass, and $\lambda(x) = \sigma_{\mathrm{sc}}(x)/[\sigma_{\mathrm{ph}}(x) + \sigma_{\mathrm{sc}}(x)]$ is the albedo for a single scattering. The 2×2 matrix, $\hat{\mathbf{R}}(x, \mu; x', \mu')$, is the azimuth-averaged polarized redistribution matrix (see Section 3).

The optical depth $\tau = 0$ at the outer (upper) boundary, and $\tau = T$ at the inner (lower) boundary. The boundary condition at the outer boundary of the slab is

$$\tilde{\boldsymbol{I}}(\tau = 0, x, -\mu) = \tilde{\boldsymbol{I}}^{\mathrm{inc}}(x, \mu), \qquad \mu > 0, \quad (2)$$

and no radiation is incident at the lower boundary.

We solve the radiative transfer equation (1) using the method based on the discrete space theory of radiative transfer (Grant & Hunt 1969a, b; Peraiah 1984; Nagendra & Peraiah 1985). This method allows us not only to determine the Stokes vector of the reflected radiation for given inci-

dent radiation, but also the global reflection matrix, i.e. Green's matrix $\hat{\mathbf{G}}(x, \mu; x', \mu')$, which makes it possible to compute economically the reflected spectrum and polarization for an arbitrary incident radiation field using

$$\tilde{\boldsymbol{I}}^{\rm ref}(x, \mu) = \tilde{\boldsymbol{I}}(\tau = 0, x, \mu) = \int_x^\infty {\rm d}x' \int_0^1 {\rm d}\mu' \hat{\mathbf{G}}(x, \mu; x', \mu') \tilde{\boldsymbol{I}}^{\rm inc}(x', \mu'), \quad \mu > 0. \tag{3}$$

The method also allows us to compute the diffuse radiation field inside the slab at chosen grid points. The details of the computation of Green's matrix are given in Appendices A and B. For the reflected flux and polarization, we use the following notations:

$$\tilde{\boldsymbol{F}}^{\rm ref}(x) = \int_0^1 \tilde{\boldsymbol{F}}^{\rm ref}(x, \mu)\, {\rm d}\mu, \quad \tilde{\boldsymbol{F}}^{\rm ref}(x, \mu) = \mu \tilde{\boldsymbol{I}}^{\rm ref}(x, \mu),$$
$$p^{\rm ref}(x, \mu) = \frac{Q^{\rm ref}(x, \mu)}{I^{\rm ref}(x, \mu)} 100 \text{ per cent}, \tag{4}$$

with similar definitions for the incident radiation identified through the superscript 'inc'.

3 REDISTRIBUTION MATRICES

In this section, we describe the redistribution mechanisms studied in this paper. The general form of the redistribution matrix employed by us is a weighted sum of redistribution matrices for classical coherent Rayleigh scattering, incoherent Compton scattering, and fluorescent line production (see Fernández et al. 1993):

$$\hat{\mathbf{R}}(x, \mu; x', \mu') = \hat{\mathbf{R}}_{\rm Rayl}(x, \mu; x', \mu') \frac{\sigma_{\rm coh}(x)}{\sigma_{\rm sc}(x)} + \hat{\mathbf{R}}_{\rm Comp}(x, \mu; x', \mu') \frac{\sigma_{\rm T}\sigma_{\rm incoh}(x)}{\sigma_{\rm KN}(x)\sigma_{\rm sc}(x)} + \hat{\mathbf{R}}_{\rm fluor}(x, \mu; x', \mu') \frac{\sigma_{\rm T}}{\sigma_{\rm sc}(x)}, \tag{5}$$

where $\sigma_{\rm KN}(x)$ is the angle-integrated Klein–Nishina cross-section for Compton scattering (e.g., Jauch & Rohrlich 1980), and $\sigma_{\rm T}$ is the Thomson scattering cross-section. We use the experimental values for $\sigma_{\rm coh}(x)$ and $\sigma_{\rm incoh}(x)$ tabulated by Hubbel et al. (1975). For $h\nu < 5$ keV, we treat the scattering as in the Rayleigh scattering approximation [i.e. $\sigma_{\rm coh}(x) = \sigma_{\rm sc}(x)$ and $\sigma_{\rm incoh}(x) = 0$].

3.1 Rayleigh redistribution matrix

The well-studied Rayleigh redistribution matrix (Chandrasekhar 1960),

$$\hat{\mathbf{R}}_{\rm Rayl}(x, \mu; x', \mu') = \delta(x - x') \times \frac{3}{16} \begin{bmatrix} 3 - \mu^2 - \mu'^2 + 3\mu^2\mu'^2 & (1 - 3\mu^2)(1 - \mu'^2) \\ (1 - \mu^2)(1 - 3\mu'^2) & 3(1 - \mu^2)(1 - \mu'^2) \end{bmatrix}, \tag{6}$$

is the coherent limit of the Compton scattering redistribution matrix at small photon energies, $x \ll 1$.

3.2 Compton redistribution matrix

The Compton redistribution matrix is given by Nagirner & Poutanen (1994)

$$\hat{\mathbf{R}}_{\rm Comp}(x, \mu; x', \mu') = \frac{3}{16\pi} \frac{x}{x'} \int_0^{2\pi} {\rm d}\varphi \delta[x' - x - xx'(1 - \cos\Theta)] \times \hat{\mathbf{P}}(x, \mu; x', \mu'; \varphi), \tag{7}$$

where

$$\hat{\mathbf{P}}(x, \mu; x', \mu'; \varphi) = \begin{bmatrix} 1 + \cos^2\Theta + w_{\rm C} & \cos^2\Theta - 1 + 2(1 - \mu^2)\sin^2\varphi \\ \cos^2\Theta - 1 + 2(1 - \mu'^2)\sin^2\varphi & 1 + \cos^2\Theta - 2(\mu^2 + \mu'^2)\sin^2\varphi \end{bmatrix}, \tag{8}$$

$w_{\rm C} = xx'(1 - \cos\Theta)^2$ is the Compton depolarization factor and Θ is the scattering angle given by

$$\cos\Theta = \mu\mu' + \sqrt{1 - \mu^2}\sqrt{1 - \mu'^2}\cos\varphi. \tag{9}$$

The Dirac δ-function in the integrand above preserves the momentum in Compton scattering. Performing the integral over φ we obtain

$$\hat{\mathbf{R}}_{\rm Comp}(x, \mu; x', \mu') = \frac{3}{8\pi} \frac{1}{x'^2 |\sin\varphi_0|} \hat{\mathbf{P}}(x, \mu; x', \mu'; \varphi_0), \quad |\cos\varphi_0| \le 1, \tag{10}$$

where

$$\varphi_0 = \cos^{-1}\left(\frac{\cos\Theta - \mu\mu'}{\sqrt{1 - \mu^2}\sqrt{1 - \mu'^2}}\right) \quad \text{and} \quad \cos\Theta = 1 - \frac{1}{x} + \frac{1}{x'}. \tag{11}$$

If $|\cos\varphi_0| > 1$ then $\hat{\mathbf{R}}_{\rm Comp}(x, \mu; x', \mu') = 0$, which causes cut-offs in the redistribution matrix at scattering angles

$$\cos\Theta_{\pm} = \mu\mu' \pm \sqrt{1 - \mu^2}\sqrt{1 - \mu'^2} \tag{12}$$

(see Fig. 1). The elements of the $\hat{\mathbf{R}}_{\rm Comp}(x, \mu; x', \mu')$ matrix satisfy the following symmetry properties:

$$R^{ij}_{\rm Comp}(x, \mu; x', \mu') = R^{ji}_{\rm Comp}(x, \mu'; x', \mu),$$
$$R^{ij}_{\rm Comp}(x, \mu; x', \mu') = R^{ij}_{\rm Comp}(x, -\mu; x', -\mu'), \quad i, j = 1, 2. \tag{13}$$

The scalar redistribution function (i.e. element 11 of the polarized redistribution matrix) satisfies the normalization condition

$$\sigma_{\rm KN}(x) = \sigma_{\rm T} \int_{x/(1+2x)}^x {\rm d}x' \int_0^1 {\rm d}\mu \int_0^1 {\rm d}\mu' \times [R^{11}_{\rm Comp}(x', \mu'; x, \mu) + R^{11}_{\rm Comp}(x', \mu'; x, -\mu)]. \tag{14}$$

The corresponding integrals over R^{12} and R^{21} are equal

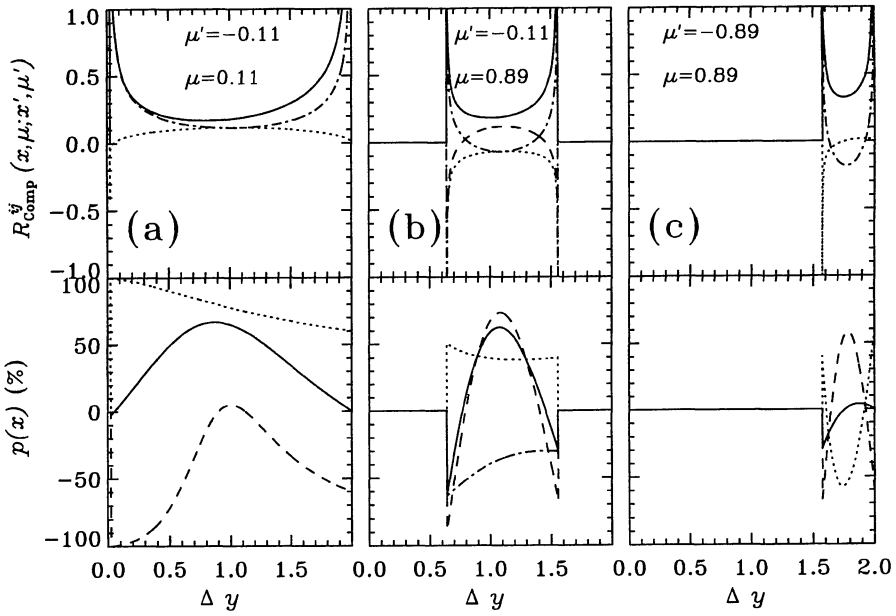

Figure 1. The polarized Compton redistribution matrix, $\hat{\mathbf{R}}_{\rm Comp}(x, \mu; x', \mu')$ (upper panels), and polarization, $p(x)$ (lower panels), of singly scattered radiation in a slab geometry. The pairs of variables, (x', μ') and (x, μ), are the energies and cosine angles of incident and scattered photons, respectively. The abscissa, $\Delta y = 1/x - 1/x' = 1 - \cos\Theta$, is the Compton wavelength shift from the original wavelength, $y' = 1/x'$, of the incident photons. Here, $x' = 1$. The 11, 12, 21 and 22 components of the polarized redistribution matrix are shown by solid, dotted, dashed and dot-dashed curves, respectively (upper panels). The polarization, $p(x)$, for three types of incident radiation: $(I', Q') = (1, 0)$, $(1, 1)$ and $(1, -1)$, are shown by solid, dotted and dashed curves, respectively. The dot-dashed curve in lower panel (b) corresponds to $(I', Q') = (1, 0)$, but for $\mu' = -0.89$ and $\mu = 0.11$.

to zero. These normalization conditions are used to check the accuracy of the numerical redistribution matrix, and thus the quality of the chosen frequency and angular grids.

In Fig. 1, we show the elements of $\hat{\mathbf{R}}_{\rm Comp}(x, \mu; x', \mu')$ for $x' = 1$ and for angles μ, μ' using a three-point Gaussian quadrature for the μ, μ' integrations. The matrix elements are plotted as a function of the dimensionless wavelength shift $\Delta y = 1/x - 1/x' = 1 - \cos\Theta$ (where $y = 1/x = \lambda/\lambda_{\rm C}$ is the dimensionless wavelength in units of the Compton wavelength, $\lambda_{\rm C} \equiv h/mc$). For $|\mu| = |\mu'|$, we have $R^{12} = R^{21}$. The function R^{11}, which represents unpolarized scalar Compton redistribution, is always positive. The polarization curves shown in the lower panels of Fig. 1 are computed using $p(x) = (Q/I)100$ per cent, where I and Q are given by

$$\begin{pmatrix} I \\ Q \end{pmatrix} = \begin{pmatrix} R^{11}_{\rm Comp} & R^{12}_{\rm Comp} \\ R^{21}_{\rm Comp} & R^{22}_{\rm Comp} \end{pmatrix} \begin{pmatrix} I' \\ Q' \end{pmatrix}, \tag{15}$$

and where (I', Q') and (I, Q) are the incident and scattered Stokes vectors, respectively. We consider three different incident Stokes vectors: (1) unpolarized incident photons, $(I', Q') = (1, 0)$; (2) 100 per cent polarization parallel to the meridian plane, $(I', Q') = (1, 1)$; and (3) 100 per cent perpendicular to the meridian plane, $(I', Q') = (1, -1)$. The corresponding scattered polarization, $p(x)$, is shown by solid, dotted and dashed curves, respectively.

For case (1) in lower panel (a), the polarization, $p(x)$, of Compton-scattered photons is zero in the (almost) forward ($\Delta y \approx 0$) and backward ($\Delta y \approx 2$) directions, and reaches a maximum $p(x)$ of ~ 67 per cent at $\cos\Theta \sim 0.1$ ($\Delta y \sim 0.9$), i.e. for scattering at nearly right angles. For cases (2) and (3), $p(x)$ is ± 100 per cent in the (almost) forward direction, but ± 60 per cent in the backward direction, where the effect of the Compton depolarization parameter, $w_{\rm C}$, is largest. In case (1), the curve would have been symmetric around $\cos\Theta = 0$ ($\Delta y = 1$) for the case of Rayleigh scattering, i.e. if $x' \ll 1$, with $p(x)$ of 100 per cent at $\Delta y = 1$. In case (3), $p(x) \approx 0$ at $\Delta y \approx 1$, as then the electric vector of the incident photons points almost in the direction of the scattered photon.

For cases (1) and (3) in lower panel (b), $p(x)$ reaches a positive maximum at $\Delta y \approx 1.1$ (corresponding to $\cos\Theta \approx -0.1$), where the scattering plane is nearly perpendicular to the meridian plane of the outgoing photons. The electric vector of the scattered photons lies in the meridian plane and $p(x)$ is positive. The negative maxima of $p(x)$ occurs when the meridian and the scattering planes coincide resulting in the scattered electric vector being perpendicular to the meridian plane. In case (2), the electric vector of the incident photons is nearly parallel to the normal, causing the scattered electric vector to be nearly parallel to the meridian plane and $p(x)$ becomes positive. In this panel we also show (dot-dashed line) the polarization produced by scattering of unpolarized incident photons from $\mu' = -0.89$ to $\mu = 0.11$. The resulting $p(x)$ is always negative owing to the scattering plane being nearly coplanar with the meridian plane of the outgoing photons as for case (1) above.

Cases (1) and (3) in panel (c) are similar to the corresponding cases in panel (b). For case (2), $p(x)$ is positive when the meridian planes coincide, and the electric vectors of the incident and scattered radiation remain in the meridian plane. Polarization changes sign when the meridian planes are perpendicular.

Evaluating $\hat{\mathbf{R}}_{\rm Comp}(x, \mu; x', \mu')$ on our pre-chosen frequency grid (see Appendix B) using equation (10) will not preserve the normalization conditions, as the matrix elements of $\hat{\mathbf{R}}_{\rm Comp}(x, \mu; x', \mu')$ vary rapidly with frequency and angle (see Fig. 1). Instead, in our radiative transfer calculations, we use a smoothed redistribution matrix obtained by averaging equation (7) over short frequency intervals $[x_{i-1/2}, x_{i+1/2}]$ with $i=1, 2, 3, \ldots, N_{\rm f}$, where $N_{\rm f}$ is the total number of points in our frequency grid:

$$\begin{aligned}
&\hat{\mathbf{R}}_{\rm Comp}(x_i, \mu; x', \mu') \\
&=\frac{3}{16\pi}\int_0^{2\pi} {\rm d}\varphi \frac{1}{A_i}\int_{x_{i-1/2}}^{x_{i+1/2}} \frac{x}{x'}\,{\rm d}x \\
&\quad\times \delta[x'-x-xx'(1-\cos\Theta)]\hat{\mathbf{P}}(x, \mu; x', \mu'; \varphi), \\
&=\frac{3}{8\pi A_i}\int_{\varphi_-}^{\varphi_+} \frac{{\rm d}\varphi}{[1+x'(1-\cos\Theta)]^2} \\
&\quad\times \hat{\mathbf{P}}\left[\frac{x'}{1+x'(1-\cos\Theta)}, \mu; x', \mu'; \varphi\right],
\end{aligned} \tag{16}$$

where A_i are the quadrature weights of frequency integration, the integration limits, $\varphi_\pm$, are

$$\cos\varphi_\pm = \left(1+\frac{1}{x'}-\frac{1}{x_\pm}-\mu\mu'\right)\Big/(\sqrt{1-\mu^2}\sqrt{1-\mu'^2}), \tag{17}$$

and

$$\begin{aligned}
x_+ &= \min\left[x_{i+1/2}, \frac{x'}{1+x'(1-\cos\Theta_+)}\right], \\
x_- &= \max\left[x_{i-1/2}, \frac{x'}{1+x'(1-\cos\Theta_-)}\right].
\end{aligned} \tag{18}$$

To achieve an accuracy of 10^{-4} in the normalization condition (14), we use 21-point Simpson quadrature when integrating over the azimuthal angle, φ, in equation (16).

3.3 Fluorescent line redistribution matrix

A fluorescent line is caused by photoelectric absorption and subsequent spontaneous radiative transitions, resulting in a redistribution of continuum photons into fluorescent line photons. This redistribution is assumed to be isotropic (and hence unpolarized, as is the case for K lines) and is described by

$$\begin{aligned}
\hat{\mathbf{R}}_{\rm fluor}(x, \mu; x', \mu') &= \tfrac{1}{2}[Y_\alpha\delta(x-x_\alpha)+Y_\beta\delta(x-x_\beta)] \\
&\quad\times\frac{\sigma_{\rm Fe}(x')}{\sigma_{\rm T}}H(x'-x_{\rm e})(1-1/J_{\rm Fe})\begin{bmatrix}1 & 0\\ 0 & 0\end{bmatrix},
\end{aligned} \tag{19}$$

where the fluorescent yields are $Y_\alpha=0.305$ and $Y_\beta=0.035$ (Kikoin 1976; Bambynek et al. 1972), for the 6.4-keV $K\alpha$ and the 7.06-keV $K\beta$ lines of Fe I, respectively, x_α and x_β are the corresponding centroid energies, $\sigma_{\rm Fe}(x)$ is the photoelectric absorption cross-section for Fe I, and $J_{\rm Fe}$ is the absorption-edge jump (see, e.g, Fernández et al. 1993). The Heaviside function, $H(x'-x_{\rm e})$, accounts for the absorption threshold at $x_{\rm e}$ (corresponding to 7.1 keV for Fe I K lines).

In equation (19) we assume that the reflecting slab is sufficiently cold (temperature <1 keV) that most of the iron is weakly ionized (see, e.g., Życki & Czerny 1994 for effects of partial ionization). Any relativistic, kinematic or thermal effects that can significantly affect the iron line profile (see, e.g., Fabian et al. 1989, Matt et al. 1991) are neglected here.

4 RESULTS AND DISCUSSION

4.1 Compton reflection for $h\nu < 5$ keV

As $\sigma_{\rm ph}(x) \gtrsim \sigma_{\rm sc}(x)$ for $h\nu < 5$ keV ($x \lesssim 0.01$), at most a few scatterings contribute to the reflected radiation. As the fractional energy decrease, $(\Delta x/x) \sim x \ll 1$, is small, the scattering can be considered as coherent, $\hat{\mathbf{R}}_{\rm Rayl}(x, \mu; x', \mu')$ can be used instead of $\hat{\mathbf{R}}(x, \mu; x', \mu')$ (see equation 5), and the transfer equation can be solved independently at each frequency.

Coherent Compton reflection for isotropic incident intensity was solved using the two-stream approximation by several authors (e.g. Lightman & White 1988), resulting in a reflected flux given by

$$F^{\rm ref}(x) = \varepsilon(x)F^{\rm inc}(x), \tag{20}$$

where

$$\varepsilon(x) = \frac{1-\sqrt{1-\lambda(x)}}{1+\sqrt{1-\lambda(x)}}. \tag{21}$$

In the general case, however, the coefficient is not simply $\varepsilon(x)$, but a Green's matrix which also depends on angles μ and μ'. We calculated Green's matrix as a function of the albedo for single scattering, $\lambda(x)$, and noticed that the ratio $[\hat{\mathbf{G}}(x, \mu; x', \mu')/\varepsilon(x)]$ is a smoothly varying function of $\lambda(x)$. This property allows us to compute the Compton-reflected spectrum at $x<0.01$ for arbitrary values of $\lambda(x)$ by interpolating between pre-tabulated values of $[\hat{\mathbf{G}}(x, \mu; x', \mu')/\varepsilon(x)]$, instead of explicitly solving the full transfer problem ab initio for each frequency point individually. We have used this quite accurate procedure when computing the <5 keV part of the spectra presented in this paper.

4.1.1 *The test case of a strongly absorbing layer*

Analytical solutions in the single-scattering approximation for $\lambda(x) \ll 1$ (e.g., Ghisellini, Haardt & Maraschi 1994, Magdziarz & Zdziarski 1995) can be used to check our numerical solutions. For $x<0.01$, Green's matrix can be expressed in terms of the redistribution matrix as

$$\hat{\mathbf{G}}(x, \mu; x', \mu') = \lambda(x)\frac{\mu'}{\mu+\mu'}\,\hat{\mathbf{R}}_{\rm Rayl}(x, \mu; x', \mu'). \tag{22}$$

We will consider three types of angular distribution of the incident radiation: (1) $F_1^{\rm inc}(x', \mu') = \delta(\mu'-\mu_0)$, i.e. radiation is incident along a cone with an opening angle $\cos^{-1}\mu_0$; (2) $F_2^{\rm inc}(x', \mu') = 1$, i.e. isotropic incident flux; and (3) $F_3^{\rm inc}(x', \mu') = 2\mu'$ corresponding to isotropic incident inten-

sity. For unpolarized incident radiation with these angular distributions we substitute equation (22) in equation (3) and obtain the angular distributions of the reflected flux in the single-scattering approximation:

$$\tilde{\boldsymbol{F}}_1^{\rm ref}(x,\mu)=\lambda(x)\frac{3}{16}\frac{\mu}{\mu+\mu_0}\begin{pmatrix}3-\mu^2-\mu_0^2+3\mu^2\mu_0^2\\(1-\mu^2)(1-3\mu_0^2)\end{pmatrix}, \tag{23}$$

$$\tilde{\boldsymbol{F}}_2^{\rm ref}(x,\mu)=$$

$$\lambda(x)\frac{3\mu}{16}\begin{pmatrix}-\frac{1}{2}(1-2\mu)(1-3\mu^2)+(3-2\mu^2+3\mu^4)\ln\frac{1+\mu}{\mu}\\(1-\mu^2)\left[-\frac{3}{2}(1-2\mu)+(1-3\mu^2)\ln\frac{1+\mu}{\mu}\right]\end{pmatrix}, \tag{24}$$

$$\tilde{\boldsymbol{F}}_3^{\rm ref}(x,\mu)=\lambda(x)\frac{\mu}{2}\begin{pmatrix}1\\0\end{pmatrix}-\mu\tilde{\boldsymbol{F}}_2^{\rm ref}(x,\mu). \tag{25}$$

In Fig. 2 we compare these analytical results (curves) as functions of viewing angle, μ, with the numerical results (squares) of our full radiative transfer calculations in the limit $\lambda(x)\ll 1$, finding excellent agreement even when using a three-point Gaussian quadrature.

For conal incident radiation, the reflected flux is larger when photons are incident along grazing angles, since these photons have a larger escape probability from the surface layer ($\tau\ll 1$) of the slab. The photons incident along the normal direction penetrate deep into the medium so that the scattered photons cannot directly escape to the surface. The polarization is always zero along the normal direction ($\mu=1$) due to the axisymmetry. In case (2), a larger number of photons are incident along grazing angles, $\mu\sim 0$, as compared to case (3) where most photons are incident close the normal. This explains the larger reflected flux in case (2). The degree of polarization behaves differently in these two cases. In case (2), the polarization is positive due to large contribution from the photons incident along the grazing angles. This is opposite to case (3), where the polarization is negative due to the large contribution from photons incident close to the normal.

4.1.2 *The test case of pure Rayleigh scattering*

We also compare our numerical results with the exact analytical solutions for conservative Rayleigh scattering [$\lambda(x)=1$] from Chandrasekhar (1960) and Sobolev (1963). The analytical Green's matrix is most simply expressed in the (I_1, I_r) basis as

$$\hat{\mathbf{G}}_{\rm l,r}(x,\mu;x',\mu')=\frac{3}{16}\frac{\mu'}{\mu+\mu'}\begin{bmatrix}S_{\rm ll}&S_{\rm lr}\\S_{\rm rl}&S_{\rm rr}\end{bmatrix}\delta(x-x'), \tag{26}$$

where the matrix elements are given by

$$\begin{aligned}S_{\rm ll}&=2H_{\rm l}(\mu)H_{\rm l}(\mu')[1-c(\mu+\mu')+\mu\mu'],\\S_{\rm lr}&=qH_{\rm l}(\mu)H_{\rm r}(\mu')(\mu+\mu'),\\S_{\rm rl}&=qH_{\rm r}(\mu)H_{\rm l}(\mu')(\mu+\mu'),\\S_{\rm rr}&=H_{\rm r}(\mu)H_{\rm r}(\mu')[1+c(\mu+\mu')+\mu\mu'],\end{aligned} \tag{27}$$

$H_{\rm l,r}$ are the well-known H-functions, $q=0.68989$ and $c=0.87294$. The final analytical results are obtained by sub-

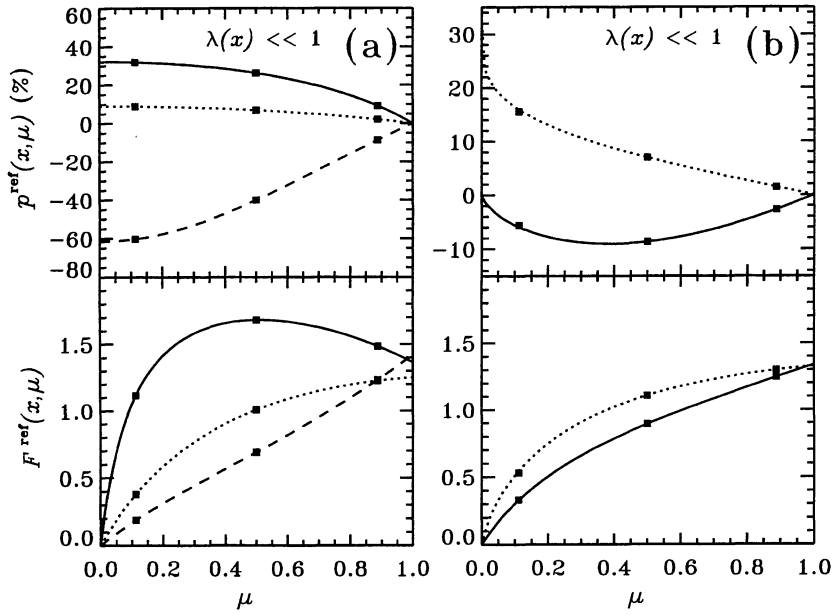

Figure 2. (a) Angular dependence of the flux, $F^{\rm ref}(x,\mu)$, and the polarization, $p^{\rm ref}(x,\mu)$, of the reflected radiation for a strongly absorbing layer with $\lambda(x)\ll 1$, and for a cone of unpolarized incident radiation given by $F_1^{\rm inc}(x',\mu')=\delta(\mu'-\mu_0)$. Curves show the results using the analytical expression (23), and squares show our numerical radiative transfer results using a three-point Gaussian quadrature ($0<\mu<1$). The solid, dotted and dashed curves show the results for $\mu_0=0.11$, 0.5 and 0.89, respectively. (b) Same as (a), but for different angular distributions of the unpolarized incident flux. Dotted curves correspond to $F_2^{\rm inc}(x',\mu')=1$ and expression (24), and solid curves to $F_3^{\rm inc}(x',\mu')=2\mu'$ and expression (25).

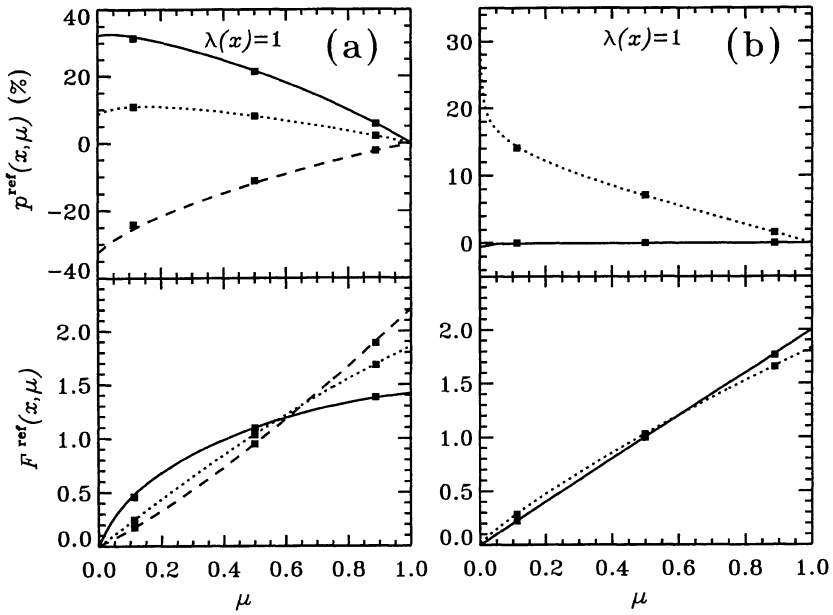

Figure 3. Same as Fig. 2 but for pure scattering, $\lambda(x)=1$. Curves show the results using the analytical expressions (26) and (27).

stituting equation (26) into equation (3) for the three cases of unpolarized incident radiation considered in Section 4.1.1.

In Fig. 3, we compare these analytical results (curves) as functions of viewing angle μ with our numerical results (squares), again finding excellent agreement. Fig. 3(a) shows the results for an unpolarized flux $F_1^{inc}(x', \mu')=\delta(\mu'-\mu_0)$ incident along a cone for three choices of $\mu_0=0.11$, 0.5 and 0.89. The reflected flux is strongly enhanced in the normal direction, and limb darkening occurs for all incident directions μ_0. The degree of polarization resembles that in Fig. 2(a) except that it is smaller for $\mu_0=0.89$ owing to the contribution of multiply scattered photons.

In Fig. 3(b), results are shown for cases (2) and (3) defined in Section 4.1.1. For both cases the reflected intensity is almost isotropic owing to the large contribution of multiply scattered photons. In case (3), the degree of polarization is very small due to an almost complete isotropy of the radiation field in the boundary layer. In case (2), the relative fraction of photons reflected close to the normal is smaller than in case (3), basically because of the dipole nature of Rayleigh scattering and because the dominant contribution to the reflected flux comes from photons incident along grazing angles. For the same reasons as in Section 4.1.1, the degree of polarization is large along the plane of the slab reaching a value of 33 per cent at $\mu=0$.

These results will be useful below when interpreting Compton reflection around 30 keV.

4.2 Compton reflection for $h\nu > 5$ keV

For $h\nu > 5$ keV ($x > 0.01$) we use the general expression (5) for the redistribution matrix. Since the radiation field at any frequency point is coupled to other frequencies through non-coherent Compton scattering, the radiative transfer equation is solved for all frequency points simultaneously (as in the case of radiative transfer in spectral lines). In order to obtain accurate solutions, we use an equally spaced wavelength grid. We will consider incident spectra as having maximum photon energies of 4 MeV, making it necessary to have a wavelength grid extending from $y \sim 100$ ($h\nu \sim 5$ keV) down to $y \sim 1/8$ ($h\nu \sim 4$ MeV). In order to accurately represent the incident and reflected spectra from 5 keV to 4 MeV we need about 400 to 800 wavelength points. We use a non-uniform wavelength grid consisting of seven regions. Each region contains 50 equally spaced wavelength points. Green's matrices on each of these wavelength regions are constructed as explained in Appendix A, and stored in memory. Green's matrix for any chosen logarithmic frequency grid is calculated and tabulated as described in Appendix B using the pre-tabulated data. We now use two tabulated Green's matrices for Compton reflection to determine the angular and spectral distributions of the reflected flux and polarization for a few cases of incident radiation with simple polarization, angular properties and spectral properties.

4.2.1 *Unpolarized isotropic monochromatic incident flux*

First, we use Green's matrix, $\mathbf{G}_2^{lin}$, (see Appendix B for notation) with a wavelength resolution of 1/4, for an unpolarized, isotropic, monochromatic incident flux, $F_2^{inc}(x', \mu')=\delta(x'-x_0)$ with $x_0=8/9$. In Fig. 4, we show the flux and polarization as a function of wavelength shift, Δy. Singly scattered radiation dominates in the region $\Delta y < 2$. The flux reflected after one scattering differs from zero for scattering angles $\cos\Theta \le \cos\Theta_{max}=\sqrt{1-\mu^2}$ (using $\mu'=0$ in equation 12). This condition sets restrictions on the wavelength shift $\Delta y \ge \Delta y_{min}=1-\sqrt{1-\mu^2}$. For viewing angles close to the plane of the slab, $\mu \sim 0$, the reflected flux is maximum for $\Delta y=2$ and ~ 0 (which correspond to the directions of forward and backward scattering and, thus, to a maximum scattering probability). In Fig. 4 the flux is non-

zero for $\Delta y = 0$, owing to our limited wavelength resolution. The degree of polarization is always positive for $\mu \sim 0$ due to large contributions from the photons incident close to the plane of the slab. It has a primary maximum at $\Delta y \sim 1$ due to contributions from photons incident perpendicular to the meridian plane of outgoing photons. For viewing angles close to the normal, $\mu \sim 1$, and for $\Delta y \sim \Delta y_{\rm min}$, only photons incident at grazing angles close to the meridian plane can contribute to $F^{\rm ref}(x, \mu)$. For such angles of incidence, the scattered radiation is polarized perpendicular to the meridian plane, and the polarization is negative.

In the region $\Delta y > 2$, the fluxes have secondary maxima at $\Delta y \sim 4$ corresponding to twice nearly back-scattered photons escaping from the slab. The secondary maxima in the polarization at $\Delta y \sim 3$ is the result of backward Compton scattering followed by a scattering at $\Theta = 90°$ (or vice versa). For larger incident photon energies, $x_0 \gg 1$, the degree of polarization is smaller because of the increase in the depolarization factor, $w_{\rm C}$, in the Compton redistribution matrix (see equations 7 and 8).

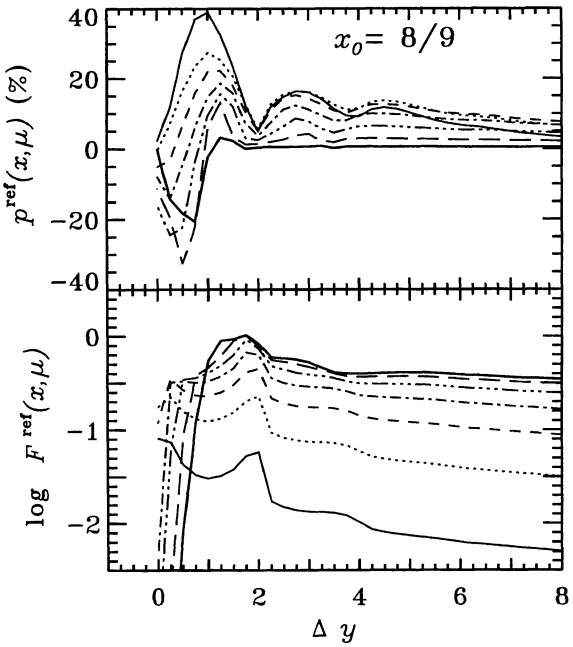

Figure 4. $F^{\rm ref}(x, \mu)$ and $p^{\rm ref}(x, \mu)$ as a function of photon wavelength shift, $\Delta y = y - y_0$, for unpolarized, isotropic, monoenergetic incident flux, $F_2^{\rm inc}(x', \mu') = \delta(x' - x_0)$, with $x_0 = 1/y_0 = 8/9$. Seven-point Gaussian angular quadrature and a wavelength resolution of 1/4 are employed. The seven curves represent seven viewing angles identified as follows: solid curves – $\mu = 0.025$; dotted curves – $\mu = 0.13$; dashed curves – $\mu = 0.30$; dot-dashed curves – $\mu = 0.50$; dot–dot–dot-dashed curves – $\mu = 0.70$; long-dashed curves – $\mu = 0.87$; and thick-solid curves – $\mu = 0.975$.

4.2.2 *Unpolarized conal incident power-law radiation*

For this and the remaining cases, we use a tabulated Green's matrix on a logarithmic frequency grid with resolution $\Delta \log x = 0.1$ (except around iron line features where we employ the original Green's matrix, $\mathbf{G}^{\rm lin}_{-1}$, with resolution $\Delta y = 2$, see Appendix B). In Fig. 5, we show the reflected flux and polarization for unpolarized incident radiation along cones of different opening angles with power-law incident spectrum, $F_1^{\rm inc}(x', \mu') = (x')^{-1}\delta(\mu' - \mu_0)$, extending up to $x' = 8$ (i.e., $h\nu' \approx 4$ MeV). For $x < 0.01$ (i.e. $h\nu < 5$ keV), we can use expression (23) to interpret the angular dependence of the Compton-reflected spectrum and polarization. Nearly constant polarization for photons incident at grazing angles (Fig. 5a) is due to the large contribution from singly scattered photons. For almost normal incidence ($\mu_0 = 0.89$), the polarization $p^{\rm ref}(x, \mu)$ decreases with frequency due to increased contribution from the multiply scattered photons (Fig. 5b). The angular dependence of $p^{\rm ref}(x, \mu)$ at $x \lesssim 0.06$

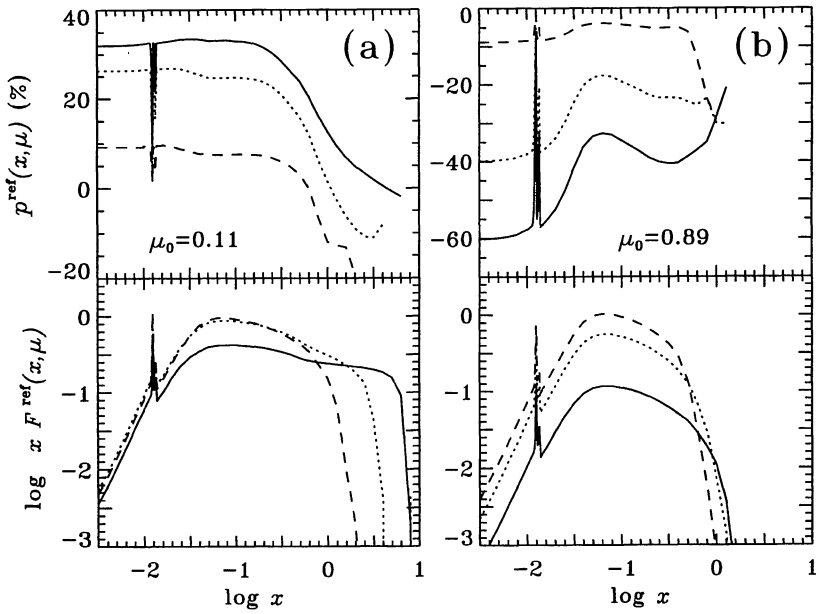

Figure 5. $F^{\rm ref}(x, \mu)$ and $p^{\rm ref}(x, \mu)$ at different viewing angles μ for an incident cone of unpolarized radiation with opening angle $\cos^{-1}\mu_0$. (a) corresponds to $\mu_0 = 0.11$ and (b) to $\mu_0 = 0.89$. The incident flux has a power-law spectrum, $F_1^{\rm inc}(x', \mu') = (x')^{-1}\delta(\mu' - \mu_0)$, extending up to $x' = 8$. The solid, dotted and dashed curves correspond to $\mu = 0.11$, 0.5 and 0.89, respectively.

($h\nu \lesssim 30$ keV) can be understood using the results for the two test cases in Section 4.1 shown by dashed curves in Figs 2(a) and 3(a). Unpolarized iron Kα and Kβ fluorescent lines cause depolarization of the continuum radiation at the corresponding line energies (see equation 19). At large photon energies, $x \gtrsim 1$, the spectra have sharp cut-offs. When $x \sim 1$, the wavelength shift $\Delta y = 1/x - 1/x' < 1$ for any value of the incident photon energy, $x' \geq x$. Here, single scattering dominates the reflected flux. For a fixed value of the incident angle, $\mu' = \mu_0$, the wavelength shift is restricted to $\Delta y \geq \Delta y_{\rm min} = 1 - \cos\Theta_+$, where $\cos\Theta_+$ is given by equation (12). This corresponds to a high-energy cut-off of the reflected spectrum at

$$x_{\rm c}(x', \mu, \mu_0) = \frac{x'}{1 + x'(1 - \cos\Theta_+)} \approx \frac{1}{1 - \cos\Theta_+} \qquad (28)$$

for $x' \gg 1$.

The degree of polarization at $x \sim 1$ is different from that at $x \sim 0.1$ due to increased contribution from the first scattering. From Fig. 5(a) we see that the degree of polarization decreases with energy, and even becomes negative in directions close to the normal. This is caused by the fact that for $\Delta y < 1$ (see Fig. 4), the polarization is positive for the radiation reflected tangentially to the layer ($\mu \sim 0$) and negative for radiation reflected in the normal direction. If the energy x of the reflected photons is close to the cut-off energy, $x_{\rm c}(x', \mu, \mu_0)$, those photons that are forward scattered in the meridian plane give the dominant contribution to the reflected radiation. In such a case, radiation scattered close to the normal directions has large negative polarization (dashed curve), but radiation scattered along the plane of the slab is nearly unpolarized (solid curve).

We compared the degree of polarization for $\mu_0 = 0.89$ (Fig. 5b) with the results of Monte Carlo computations by Matt (1993, see his fig. 3, which shows the degree of polarization in the broad energy bands $h\nu < 10$ keV, $h\nu = 10$–30 keV and $h\nu = 30$–50 keV) and estimated the relative difference to be at most 10 per cent.

4.2.3 Unpolarized isotropic power-law incident flux and intensity

Fig. 6(a) shows reflected spectra for unpolarized isotropic incident flux having a power-law distribution in energy, $F_2^{\rm inc}(x', \mu') = (x')^{-1}$, extending up to $x' = 8$. The reflected flux and polarization for $x < 0.01$ can be interpreted using equation (24) for single scattering in a layer with dominant absorption. The angular dependence for this frequency region is shown in Fig. 2(b) (dotted curves). At energies $x \sim 0.05$, multiple scatterings dominate the transfer of radiation, and the results can be interpreted using equations (26) and (27). The angular dependence in this region of the spectrum is shown in Fig. 3(b) (the dotted curves). The cut-off energy for monoenergetic incident photons is given by equation (28) with $\mu' = 0$ (Hua & Lingenfelter 1992). The energy dependence of polarization is similar to that shown in Fig. 5(a). This is due to a strong contribution to the reflected radiation from photons incident at grazing angles.

For the incident radiation of the form $F^{\rm inc}(x', \mu') = \exp(-x')/x'$, we compared the reflected flux with the results of Magdziarz & Zdziarski (1995). The largest deviation ~ 6 per cent is consistent with the accuracy of both methods. We also compared the Fe line equivalent width with the results of George & Fabian (1991). Our calculations give values ~ 10 per cent smaller due to the smaller photoelectric absorption adopted by us (see Życki & Czerny 1994).

Fig. 6(b) shows reflected spectra for unpolarized incident radiation of the form $F_3^{\rm inc}(x', \mu') = 2\mu'(x')^{-1}$. For $x < 0.01$ and at $x \sim 0.05$, the angular dependence of the reflected flux and polarization is similar to those shown in Figs 2(b) and 3(b) (solid curves). The angular and frequency dependence

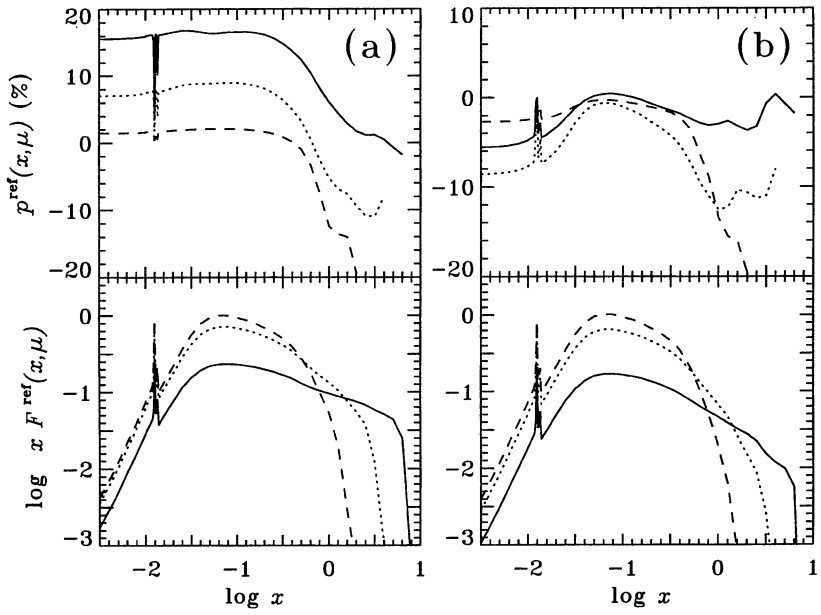

Figure 6. Same as Fig. 5, but with unpolarized incident power-law spectra of the form $F_2^{\rm inc}(x', \mu') = (x')^{-1}$ for panel (a), and $F_3^{\rm inc}(x', \mu') = 2\mu'(x')^{-1}$ for panel (b).

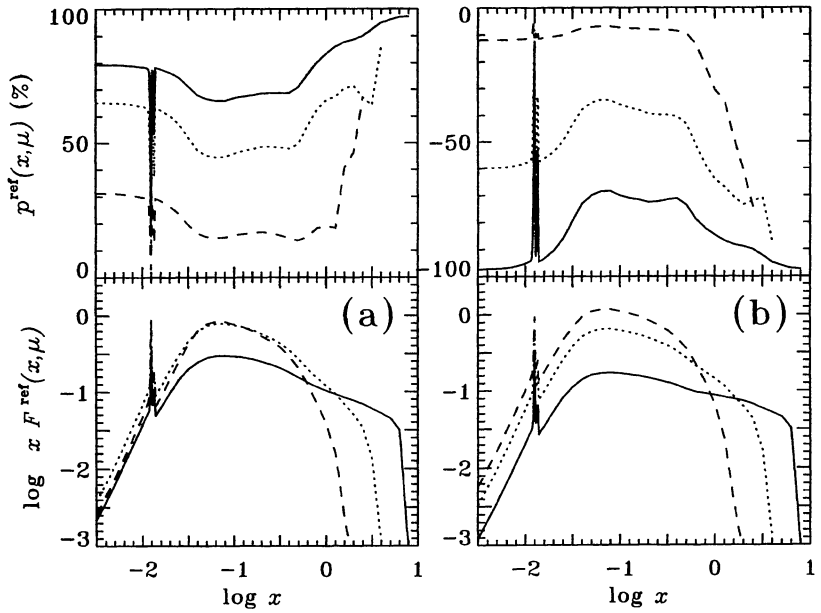

Figure 7. Same as Fig. 6(a) (i.e. isotropic incident flux with a power-law spectrum) but for incident polarization of +100 per cent in panel (a); and for incident polarization −100 per cent in panel (b).

of $F^{ref}(x, \mu)$ and $p^{ref}(x, \mu)$ at very high energies ($x \gtrsim 1$) in Fig. 6(b) is qualitatively the same as in Fig. 6(a).

Polarization at high energies has complex behaviour reflecting the 'waves' in polarization occurring at approximately the same photon energies for incident radiation of any $x' \gg 1$ (see Fig. 4). Sharp kinks are caused by poor resolution of the angular grid.

4.2.4 Polarized isotropic power-law incident flux and intensity

Figs 7(a) and (b) are similar to Fig. 6(a), except that now the polarization of the incident radiation is +100 and −100 per cent, respectively. The flux profiles in Figs 7(a) and (b) are sensitive to the degree of incident polarization. Indeed, the spectra in Fig. 6(a) are weighted averages of these two extreme cases. We emphasize that for highly polarized incident radiation it is necessary to consider the transfer of polarized radiation in order to get correct estimates of $F^{ref}(x, \mu)$ and $p^{ref}(x, \mu)$. The polarization is nearly constant for $0.03 < x < 0.5$ where multiply Compton-scattered photons dominate. The sharp increase of polarization for $x > 0.5$ is due to the strong contribution of singly scattered photons. As already mentioned, the Compton depolarization factor, w_C, and thus the singly scattered polarization depend strongly on the scattering angle Θ. Photons at high energies are nearly forward scattered where the depolarization is minimum. Thus, the polarization is ±100 per cent at large energies in Figs 7(a) and (b).

5 SUMMARY

A numerical method based on discrete space theory in order to solve polarized Compton scattering problems was presented. This method was employed to solve the problem of Compton reflection of incident X-rays and γ-rays by an optically thick planar slab of cold neutral matter accounting for both photoelectric absorption and the generation of a fluorescent Fe line. The relevant transfer equation was written in the (I, Q) basis in order to solve the Compton reflection problem in an axially symmetric situation. Generalization to non-axial symmetries is also possible. Explicit expressions were given for the Compton redistribution matrix for cold matter.

We discussed the basic physics of Compton frequency redistribution as a non-coherent mechanism. The scattering of X-rays with photon energies < 5 keV can be well described using the Rayleigh scattering limit. For larger photon energies > 5 keV, the Compton redistribution matrix must be used. Common features and differences between Rayleigh and Compton redistributions were described quantitatively, and analytical methods and simple numerical approximations were used to understand the radiative transfer results. The emergent reflected spectra and polarization for a variety of incident radiation fields were presented and discussed.

Green's matrix for the Compton reflection problem was computed and stored. The tabulated Green's matrices are available electronically from the authors.

ACKNOWLEDGMENTS

This research was partially supported by a grant from the Swedish Natural Science Research Council. KNN is grateful to the Stockholm Observatory for its kind hospitality during his visit in 1995 August.

REFERENCES

Bambynek W. et al., 1972, Rev. Mod. Phys., 44, 716
Burigana C., 1995, MNRAS, 272, 481
Chandrasekhar S., 1960, Radiative Transfer. Dover, New York

Done C., Mulchaey J. S., Mushotzky R. F,. Arnaud K. A., 1992, ApJ, 395, 275
Fabian A., Rees M. J., Stella L., White N. E., 1989, MNRAS, 238, 729
Fernández J. E., Hubbel J. H., Hanson A. L., Spencer L. V., 1993, Radiat. Phys. Chem., 41, 579
George I. M., Fabian A. C., 1991, MNRAS, 249, 352
Ghisellini G., Haardt F., Matt G., 1994, MNRAS, 267, 743
Grant I. P., Hunt G. E., 1969a, Proc. R. Soc. Lond. A, 313, 183
Grant I. P., Hunt G. E., 1969b, Proc. R. Soc. Lond. A, 313, 199
Haardt F., Maraschi L., 1993, ApJ, 413, 507
Haardt F., Done C., Matt G., Fabian A. C., 1993, ApJ, 411, L95
Hua X.-M., Lingenfelter R. E., 1992, ApJ, 397, 591
Hubbel J. H. et al., 1975, J. Phys. Chem. Ref. Data, 4, 471
Illarionov A., Kallman T., McCray R., Ross R., 1979, ApJ, 228, 279
Jauch J. M., Rohrlich F., 1980, The Theory of Photons and Electrons, 2nd edn. Springer-Verlag, New York
Kikoin I. K., ed., 1976, Tables of Physical Quantities. Atomizdat, Moscow
Lightman A. P., White T. R., 1988, ApJ, 335, 57
Lightman A. P., Lamb D. Q., Rybicki G. B., 1981, ApJ, 248, 738
Magdziarz P., Zdziarski A., 1995, MNRAS, 273, 837
Matt G., 1993, MNRAS, 260, 663
Matt G., Perola G. C., Piro L., 1991, A&A, 247, 25
Morrison R., McCammon D., 1983, ApJ, 270, 119
Nagendra K. N., Peraiah A., 1985, MNRAS, 214, 203
Nagirner D. I., Poutanen J., 1994, in Sunyaev R. A., ed., Astrophys. Space Phys. Reviews, Vol. 9. Harwood, New York, p. 1
Nandra K., Pounds K. A., 1994, MNRAS, 268, 405
Peraiah A., 1984, in Kalkofen W., ed., Methods in Radiative Transfer. Cambridge Univ. Press, Cambridge, p. 281
Pounds K. A., Nandra K., Stewart G. C., George I. M., Fabian A. C., 1990, Nat, 344, 132
Sobolev V. V., 1963, A Treatise on Radiative Transfer. Van Nostrand, New York
Stern B. E., Poutanen J., Svensson R., Sikora M., Begelman M. C., 1995, ApJ, 449, L13
White T. R., Lightman A. P., Zdziarski A. A., 1988, ApJ, 331, 939
Zdziarski A. A., Fabian A. F., Nandra K., Celotti A., Rees M. J., Done C., Coppi P. S., Madejski G. M., 1994, MNRAS, 269, L55
Zdziarski A. A., Johnson W. N., Magdziarz P., 1996, MNRAS, 283, 193
Życki P. T., Czerny B., 1994, MNRAS, 266, 653

APPENDIX A: A BRIEF ACCOUNT OF THE POLARIZED RADIATIVE TRANSFER ALGORITHM

We employ the method of solution given by Grant & Hunt (1969a,b). It is a discrete ordinate finite difference method. Consider a plane-parallel slab of total thickness T with radiation incident only on the upper boundary ($\tau=0$). For convenience, we assume that there are no sources of radiation inside the slab. Let $x_i (i=1, N_f)$ be the set of frequency points and $\mu_j=\cos\theta_j$ $(j=1,J)$ be the angle cosines in the interval [0, 1]. The Stokes vector at an optical depth τ_n is written as a vector of $2N_fJ$ elements and is denoted by $\mathbf{I}_n^{\pm}$ with + and − signs denoting the upward and downward directions, respectively. More specifically, the elements of the intensity vector are $I_{n,k}^{\pm}=I(\tau_n, x_i, \pm\mu_j)$ and $I_{n,k+N_fJ}^{\pm}=Q(\tau_n, x_i, \pm\mu_j)$, with the running index k given by $k=j+J(i-1)$.

The medium is divided into N layers of arbitrary optical thickness. Consider now an arbitrary layer (n, m) bounded by the planes τ_n and τ_m, such that $0\le\tau_n<\tau_m\le T$ with $m=n+1$ and $n=1, 2, \ldots, N$. Let the Stokes vectors incident on this layer be $\mathbf{I}_m^+$ and $\mathbf{I}_n^-$. If the emerging Stokes vectors, $\mathbf{I}_n^+$ and $\mathbf{I}_m^-$, depend linearly on the incident radiation, then we can write

$$\begin{bmatrix}\mathbf{I}_n^+\\ \mathbf{I}_m^-\end{bmatrix}=\mathbf{S}(n,m)\begin{bmatrix}\mathbf{I}_m^+\\ \mathbf{I}_n^-\end{bmatrix}, \tag{A1}$$

where the interaction matrix, $\mathbf{S}(n, m)$, is given by

$$\mathbf{S}(n,m)=\begin{bmatrix}\mathbf{t}(n,m) & \mathbf{r}(m,n)\\ \mathbf{r}(n,m) & \mathbf{t}(m,n)\end{bmatrix}. \tag{A2}$$

The linear operators $\mathbf{t}(n, m)$, $\mathbf{t}(m, n)$ and $\mathbf{r}(n, m)$, $\mathbf{r}(m, n)$ describing diffuse transmission and diffuse reflection of radiation can also be defined as integral operators. For example, for the reflection matrix $\mathbf{r}(m, n)$ we can write

$$\mathbf{r}(m,n)\mathbf{I}_n^- =\int_0^\infty \mathrm{d}x' \int_0^1 \mathrm{d}\mu' r(\tau_m, x, \mu; \tau_n, x', -\mu') \times \tilde{\boldsymbol{I}}(\tau_n, x', -\mu'), \qquad 0<\mu\le 1. \tag{A3}$$

In the discrete ordinate representation, $\mathbf{r}(m, n)$ is a $2N_fJ\times 2N_fJ$ matrix. The integrals in the above equation are performed using angular and frequency quadratures with weights, c_j and A_i, respectively.

We now give the expressions for determining the fluxes emerging from a homogeneous slab. Consider two adjacent layers bounded by planes at τ_n, τ_m and τ_p, where $0\le\tau_n<\tau_m<\tau_p\le T$. Using equation (A1) we can write

$$\begin{bmatrix}\mathbf{I}_n^+\\ \mathbf{I}_m^-\end{bmatrix}=\mathbf{S}(n,m)\begin{bmatrix}\mathbf{I}_m^+\\ \mathbf{I}_n^-\end{bmatrix} \quad\text{and}\quad \begin{bmatrix}\mathbf{I}_m^+\\ \mathbf{I}_p^-\end{bmatrix}=\mathbf{S}(m,p)\begin{bmatrix}\mathbf{I}_p^+\\ \mathbf{I}_m^-\end{bmatrix}. \tag{A4}$$

Since τ_n, τ_m and τ_p are arbitrary, we can also write

$$\begin{bmatrix}\mathbf{I}_n^+\\ \mathbf{I}_p^-\end{bmatrix}=\mathbf{S}(n,p)\begin{bmatrix}\mathbf{I}_p^+\\ \mathbf{I}_n^-\end{bmatrix}. \tag{A5}$$

The matrix $\mathbf{S}(n, p)$ can be written as a 'star-product' of two interaction matrices for the adjacent layers as

$$\mathbf{S}(n,p)=\mathbf{S}(n,m)*\mathbf{S}(m,p), \tag{A6}$$

where the elements of the interaction matrix $\mathbf{S}(n, p)$ for the composite layer can be found by eliminating $\mathbf{I}_m^{\pm}$ from the set of equations (A4):

$$\begin{aligned}
&\mathbf{t}(n,p)=\mathbf{t}(n,m)[\mathbf{E}-\mathbf{r}(p,m)\mathbf{r}(n,m)]^{-1}\mathbf{t}(m,p),\\
&\mathbf{t}(p,n)=\mathbf{t}(p,m)[\mathbf{E}-\mathbf{r}(n,m)\mathbf{r}(p,m)]^{-1}\mathbf{t}(m,n),\\
&\mathbf{r}(n,p)=\mathbf{r}(m,p)+\mathbf{t}(p,m)\mathbf{r}(n,m)\\
&\qquad\times[\mathbf{E}-\mathbf{r}(p,m)\mathbf{r}(n,m)]^{-1}\mathbf{t}(m,p),\\
&\mathbf{r}(p,n)=\mathbf{r}(m,n)+\mathbf{t}(n,m)\mathbf{r}(p,m)\\
&\qquad\times[\mathbf{E}-\mathbf{r}(n,m)\mathbf{r}(p,m)]^{-1}\mathbf{t}(m,n),
\end{aligned} \tag{A7}$$

where $\mathbf{E}$ denotes the identity operator. The physical meaning of these equations as well as properties of the 'star-product' can be found in Grant & Hunt (1969a,b).

The discrete ordinate representation of the transfer equation (1) is given by

$$\mathbf{M}\frac{d\mathbf{I}_n^+}{d\tau}+\mathbf{I}_n^+=\lambda[\mathbf{R}^{++}\mathbf{c}\mathbf{I}_n^+ +\mathbf{R}^{+-}\mathbf{c}\mathbf{I}_n^-],$$
$$\mathbf{M}\frac{d\mathbf{I}_n^-}{d\tau}-\mathbf{I}_n^+=\lambda[\mathbf{R}^{-+}\mathbf{c}\mathbf{I}_n^+ +\mathbf{R}^{--}\mathbf{c}\mathbf{I}_n^-], \tag{A8}$$

where $\mathbf{M}$, $\mathbf{c}$ and λ are $2N_fJ\times 2N_fJ$ diagonal matrices, with the elements given by

$$M_{qq'}=\mu_j\delta_{qq'},\quad c_{qq'}=c_jA_i\delta_{qq'},\quad \lambda_{qq'}=\lambda(x_i)\delta_{qq'}. \tag{A9}$$

The matrices $\mathbf{R}^{\pm\pm}$ are discrete ordinate representations of the redistribution matrix, with the elements written explicitly as

$$R_{qq'}^{\pm\pm}=\frac{x_i}{x_{i'}}\,R_{ll'}(x_i,\ \pm\mu_j;\ x_{i'},\ \pm\mu_{j'}). \tag{A10}$$

The indices q and q' are given by $q=j+J[i-1+N_f(l-1)]$; and $q'=j'+J[i'-1+N_f(l'-1)]$. The polarization indices $l, l'=1, 2$. By reducing the discretized transfer equations to the canonical form (equation A5) through straightforward algebraic manipulations, we obtain expressions for the transmission and reflection matrices:

$$\begin{aligned}\mathbf{t}(n,m)&=\mathbf{E}-h\mathbf{M}^{-1}(\mathbf{E}-\lambda\mathbf{R}^{++}\mathbf{c})+o(h),\\ \mathbf{t}(m,n)&=\mathbf{E}-h\mathbf{M}^{-1}(\mathbf{E}-\lambda\mathbf{R}^{--}\mathbf{c})+o(h),\\ \mathbf{r}(n,m)&=h\mathbf{M}^{-1}(\mathbf{E}-\lambda\mathbf{R}^{+-}\mathbf{c})+o(h),\\ \mathbf{r}(m,n)&=h\mathbf{M}^{-1}(\mathbf{E}-\lambda\mathbf{R}^{-+}\mathbf{c})+o(h),\end{aligned} \tag{A11}$$

where the step-size $h=\tau_m-\tau_n$. Through successive applications of the star-product (see equation A6), we can build up the global 'transfer operator' $\mathbf{S}(1, N+1)$ which represents the transfer of radiation throughout the entire slab. Finally, we can obtain the external response (emergent intensities) from the slab by using equation (A1) with $n=1, m=N+1$. This procedure is useful for slabs which are homogeneous and/or optically thin ($\tau\sim 1$). In such cases, we can employ uniform or logarithmic depth grids with $N=50$–100 points to develop accurate $\mathbf{t}$ and $\mathbf{r}$ matrices for the whole slab. If the medium is optically thick and inhomogeneous, the $\mathbf{t}$ and $\mathbf{r}$ operators for layers of arbitrary thickness are preferably computed by a fast doubling procedure. The discussion on the accuracy and stability of this method can be found in Grant & Hunt (1969b) and Peraiah (1984). The algorithm is stable as long as a step-size criterion

$$h\le\tau_{cr}=\min\frac{2\mu_j}{1-2\lambda(x_i)R_{qq'}^{\pm\pm}c_j} \tag{A12}$$

is satisfied.

We now show how to compute the Stokes vectors $\mathbf{I}_n^{\pm}$ at the selected levels, $0=\tau_1<\ldots\tau_n<\tau_{n+1}<\ldots<\tau_{N+1}=T$, within the medium. First, the matrices $\mathbf{S}(n, n+1)$ are computed using the methods described above, and stored in memory. Then, we compute by forward elimination for $n=1, 2, \ldots, N$ the auxiliary quantities, $\mathbf{r}(1, n)$ and $\mathbf{V}_{n+1/2}^{\pm}$, starting with initial conditions, $\mathbf{r}(1, 1)=0$, and $\mathbf{V}_{1/2}^-=\mathbf{I}_1^-$. Notice that $\mathbf{I}_1^-$ is the radiation field incident at the top boundary ($\tau=0$), which is specified as a boundary condition. The elimination procedure is formally written as

$$\begin{aligned}\mathbf{r}(1,n+1)=\mathbf{r}(n,n+1)+\mathbf{t}(n+1,n)\mathbf{r}(1,n)\\ \times[\mathbf{E}-\mathbf{r}(n+1,n)\mathbf{r}(1,n)]^{-1}\mathbf{t}(n,n+1),\end{aligned} \tag{A13}$$

and

$$\begin{aligned}\mathbf{V}_{n+1/2}^-&=\hat{\mathbf{t}}(n+1,n)\mathbf{V}_{n-1/2}^-,\\ \mathbf{V}_{n+1/2}^+&=\hat{\mathbf{r}}(n+1,n)\mathbf{V}_{n-1/2}^-,\end{aligned} \tag{A14}$$

where the $\hat{\mathbf{t}}$ and $\hat{\mathbf{r}}$ operators are computed using

$$\begin{aligned}\hat{\mathbf{t}}(n+1,n)&=\mathbf{t}(n+1,n)[\mathbf{E}-\mathbf{r}(1,n)\mathbf{r}(n+1,n)]^{-1},\\ \hat{\mathbf{r}}(n+1,n)&=\mathbf{r}(n+1,n)[\mathbf{E}-\mathbf{r}(1,n)\mathbf{r}(n+1,n)]^{-1}.\end{aligned} \tag{A15}$$

Finally, we compute recursively by backsubstitution, the radiation field $\mathbf{I}_{n+1}^-$ and $\mathbf{I}_n^+$ for all layers of the medium, $n=N, N-1, \ldots, 2, 1$, including the boundaries. This reverse sweep is performed starting with the boundary condition $\mathbf{I}_{N+1}^+=\mathbf{I}^+(\tau=T)$ at the lower boundary [in this paper, we use $\mathbf{I}^+(\tau=T)=0$]. The required equations are

$$\mathbf{I}_{n+1}^-=\mathbf{r}(1,n+1)\mathbf{I}_{n+1}^+ +\mathbf{V}_{n+1/2}^-$$

and (A16)

$$\mathbf{I}_n^+=[\mathbf{E}-\mathbf{r}(n+1,n)\mathbf{r}(1,n)]^{-1}\mathbf{t}(n,n+1)\mathbf{I}_{n+1}^+ +\mathbf{V}_{n+1/2}^+.$$

It is important to recognize the fact that the global reflection matrix $\mathbf{r}(1, N+1)$ in equation (A13) is nothing but Green's matrix for the 'reflection of radiation', incident at the top of the slab:

$$\mathbf{G}=\mathbf{r}(1,N+1) \tag{A17}$$

This non-local operator $\mathbf{G}$ contains the multiple scattering contributions of all scattering orders. It accounts for the contribution of scattered photons from all directions and from all spatial points in the slab. This can be clearly seen by expanding $[\mathbf{E}-\mathbf{r}(n+1, n)\mathbf{r}(1, n)]^{-1}$ in equation (A13) to the first few terms. It turns out that the single scattering approximation and the method of expansion in scattering orders form limiting cases of the general method of solving the transfer equation presented above.

APPENDIX B: CONSTRUCTION OF GREEN'S MATRIX ON AN ARBITRARY FREQUENCY GRID

Since incident theoretical spectra are computed on a logarithmic frequency grid, we present a simple technique for obtaining Green's matrix $\mathbf{G}^{log}$ on a logarithmic grid (log-grid). Green's matrices, $\mathbf{G}^{lin}$, that we originally compute using equation (A17), are evaluated on an equally spaced (linear) wavelength grid and stored. The $\mathbf{G}^{log}$ matrix is, however, required on a log-grid, but it cannot be obtained from $\mathbf{G}^{lin}$ by simple interpolations, because the matrix functions are highly peaked in angle and frequency variables. In the radiative transfer solution of the Compton reflection problem, we need an equally spaced wavelength grid. The wavelength step-size, Δy, must always be less than 2, otherwise scattered photons are not transmitted from one wavelength grid point to the next. However, it is practically impossible from a computational viewpoint to cover the large energy range, $0.01<x<10$, using a single step-size. Instead we use

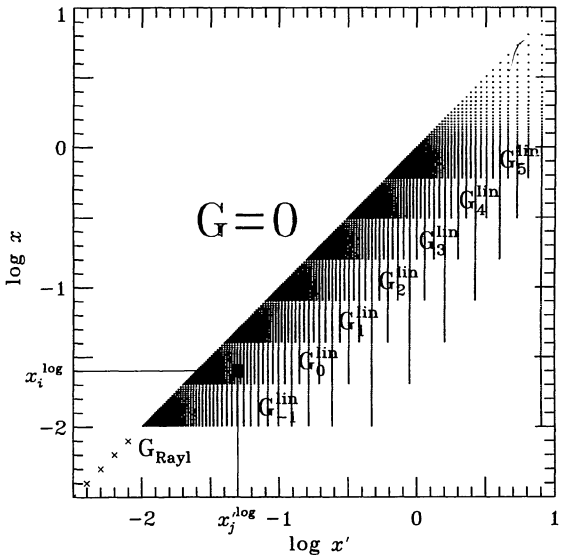

Figure B1. The equally spaced wavelength grids on which Green's matrices for Compton reflection are computed and stored. All wavelength grids start at the rightmost vertical line, $x'=8$. $\mathbf{G}_k^{\rm lin}$ ($k=-1,\ldots,5$) represent high-energy Compton scattering regime. As $x'\geq x$ for Compton scattering on cold matter, $\mathbf{G}=0$ above the diagonal. The black square shows the area over which $\mathbf{G}_k^{\rm lin}$ values are averaged in order to obtain the value of $\mathbf{G}^{\rm log}$ at $(x_i^{\rm log}, x_j'^{\rm log})$. $\mathbf{G}_{\rm Rayl}$ represents the Rayleigh scattering regime shown by the crosses.

seven grids with different step-sizes which start at the same wavelength point, $y_0=1/8$ (i.e. $h\nu_0\approx 4$ MeV), and cover different ranges in energy as seen in Fig. B1. The wavelength point i for the grid k is given by the formula

$$y_{k,i}=y_0+(i-1)\Delta y_k,$$
$$i=1,\ldots,N_{\rm f} \quad \text{and} \quad k=-1,\ldots,N_{\rm G},$$

where the step-size $\Delta y_k=2^{-k}$. In this paper we have used $N_{\rm f}=50$ and $N_{\rm G}=5$ to calculate the $\mathbf{G}_k$ matrices. Fig. B1 shows the actual grids on which the $\mathbf{G}_k^{\rm lin}$ matrices are computed and stored. Each vertical line represents a wavelength grid. Since $x'\geq x$ for Compton scattering on cold matter, we have $\mathbf{G}=0$ for $x'<x$, and we need to store $\mathbf{G}_k^{\rm lin}$ matrices only for half of the (x,x') plane. To determine the $\mathbf{G}^{\rm log}$ matrix on a log-grid at a point $(x_i^{\rm log}, x_j'^{\rm log})$, we perform an average of $\mathbf{G}_k^{\rm lin}$ over a square with boundaries $[x_{i-1/2}^{\rm log}, x_{i+1/2}^{\rm log}]$ and $[x_{j-1/2}'^{\rm log}, x_{j+1/2}'^{\rm log}]$ centred at the point $(x_i^{\rm log}, x_j'^{\rm log})$. This averaging takes into account the typical incident spectrum, $I^{\rm inc}(x)\propto x^{-1}$. Applying a different incident spectrum power-law gives differences in the reflected spectrum of order ~ 0.1 per cent, which are much less than the overall accuracy of the calculations.

Calculation of the $\mathbf{G}^{\rm log}$ matrix for $x=x'<0.01$ (Rayleigh scattering regime) can be performed by a trivial interpolation of $\lambda(x)$, since Green's matrix now depends only on $\lambda(x)$ (see Section 4.1 and the lower left corner of Fig. B1).

The relative accuracy in the evaluation of the reflected spectra depends on the resolution of the grids used for computing $\mathbf{G}_k^{\rm lin}$. We found that for very hard incident spectra (with energy power-law index $\alpha<0$), the final errors in the reflected spectrum are ~ 20 per cent. We can easily reduce these errors by choosing wavelength grids with higher resolution and/or increasing the number of frequency grid points. For incident softer spectra ($\alpha>0.5$), the errors are less than 6 per cent. The errors related to the discrete space method depend on the accuracy that the normalization condition (14) satisfies (Grant & Hunt 1969b; Nagendra & Peraiah 1985). For the case of Compton scattering, we have a sink of photons at the low-energy boundary of the grid, and the normalization condition cannot be satisfied at this grid boundary. We estimated the final errors in the reflected spectra by comparing spectra computed using different $\mathbf{G}_k^{\rm lin}$.